

Quantifying galaxy shapes: Sérsiclets and beyond

René Andrae^{1*}, Peter Melchior^{2,3,4} and Knud Jahnke¹

¹*Max-Planck-Institut für Astronomie, Königstuhl 17, 69117 Heidelberg, Germany*

²*Institut für Theoretische Astrophysik, Zentrum für Astronomie, Albert-Ueberle-Str. 2, 69120 Heidelberg, Germany*

³*Center for Cosmology and Astro-Particle Physics, The Ohio State University, 191 W. Woodruff Ave., Columbus, Ohio 43210, USA*

⁴*Department of Physics, The Ohio State University, 191 W. Woodruff Ave., Columbus, Ohio 43210, USA*

Accepted 2011 June 28. Received 2011 February 22.

ABSTRACT

Parametrisation of galaxy morphologies is a challenging task, for instances in shear measurements of weak gravitational lensing or investigations of formation and evolution of galaxies. The huge variety of different morphologies requires a parametrisation scheme that is highly flexible and that accounts for certain morphological observables, such as ellipticity, steepness of the radial light profile and azimuthal structure. In this article, we revisit the method of sérsiclets, where galaxy morphologies are decomposed into a set of polar basis functions that are based on the Sérsic profile. This approach is justified by the fact that the Sérsic profile is the first-order Taylor expansion of any real light profile. We show that sérsiclets indeed overcome the modelling failures of shapelets in the case of early-type galaxies. However, sérsiclets implicate an unphysical relation between the steepness of the light profile and the spatial scale of the polynomial oscillations, which is not necessarily obeyed by real galaxy morphologies and can therefore give rise to modelling failures. Moreover, we demonstrate that sérsiclets are prone to undersampling, which restricts sérsiclet modelling to highly resolved galaxy images. Analysing data from the weak-lensing GREAT08 challenge, we demonstrate that sérsiclets should not be used in weak-lensing studies. We conclude that although the sérsiclet approach appears very promising at first glance, it suffers from conceptual and practical problems that severely limit its usefulness. In particular, sérsiclets do not provide high precision results in weak-lensing studies. Finally, we show that the Sérsic profile can be enhanced by higher-order terms in the Taylor expansion, which can drastically improve model reconstructions of galaxy images. When orthonormalised, these higher-order profiles can overcome the problems of sérsiclets while preserving their mathematical justification. However, this method is computationally expensive.

Key words: Galaxies: general – Methods: data analysis, statistical – Techniques: image processing – Gravitational lensing: weak.

1 INTRODUCTION

There are two scientific key diagnostics in modern investigations of galaxy formation and evolution, namely star-formation rates and galaxy morphologies. Galaxy morphologies are known to correlate to different degrees with other more physical parameters such as star formation (e.g., Kennicutt 1998) or environment (e.g., van der Wel et al. 2010). Although morphology by itself is not a fundamental parameter of a galaxy, it provides a direct observable. Conversely, e.g., star-formation rates are derived quantities based on additional assumptions and extrapolations (e.g., Rosa-González et al. 2002). Studies of galaxy morphologies are therefore an important complementary means for

studying the physics of galaxy formation. Furthermore, certain investigations are solely based on morphologies, e.g., weak-lensing measurements (e.g., Bernstein & Jarvis 2002) or studies of angular-momentum alignments of spiral galaxies (e.g., Slosar et al. 2009; Andrae & Jahnke in prep.). Concerning weak gravitational lensing, the investigation of shape-measurement algorithms currently is a very active and important field of research since established and well known procedures fail to measure object shapes accurately enough to fully exploit the potential of future large-scale imaging surveys (e.g. Bridle et al. 2010; Bernstein 2010). Concerning morphological classification, galaxies were traditionally described mostly by visual classifications. However, given the enormous amount of galaxies known from today’s sky surveys, it is evident that an automated *parametrisation* of galaxy morphologies is required. Consequently, there has

* E-mail: andrae@mpia-hd.mpg.de

been substantial effort to define automated parametrisation schemes for galaxy morphologies (e.g., Sérsic 1968; Abraham et al. 1996, 2003; Bershadsky et al. 2000; Conselice 2003; Lotz et al. 2004, 2008, to name just a few). Unfortunately, these parametrisation schemes usually invoke rather restrictive assumptions, such that they lack the flexibility to describe the huge variety of different galaxy morphologies present in modern databases (Andrae et al. 2010a). The Sérsic profile (Sérsic 1968) is one example in this respect: The Sérsic model is the first-order Taylor expansion of any real radial light profile (cf. Appendix A1) and therefore provides a good first-order approximation to real galaxies. However, second-order effects – e.g., deviations of the radial profile from the Sérsic form or the appearance of azimuthal structures such as star-forming regions, galactic bars or spiral-arm patterns – are typically not negligible, and hence there have been several attempts to enhance the Sérsic profile:

- Mixtures of two or more Sérsic profiles (e.g. Simmat et al. 2010).
- Modification of the Sérsic profile by Fourier modes in order to describe azimuthal structures (e.g., GALFIT 3, Peng et al. 2010).
- Orthogonalisation of the Sérsic profile in order to describe azimuthal structures (Ngan et al. 2009).

The idea of using basis functions in order to parametrise galaxy morphologies is not new. For instances, “shapelets” (Réfrégier 2003) are a set of basis functions based on the Gaussian profile. The appealing properties of shapelets gave rise to a number of investigations of galaxy morphologies (e.g., Kelly & McKay 2004, 2005; Andrae et al. 2010b) and weak-lensing studies (e.g., Massey et al. 2007; Ferry et al. 2008). However, as was recently shown by Melchior et al. (2010), shapelets can suffer from strong biases that originate from the radial light profiles of galaxies potentially being much steeper than a Gaussian profile, in particular for early-type galaxies. These biases manifest themselves as ring-like artefacts in the models and the residual maps (cf. Sect. 3.2). They are able to wash out virtually all the information about ellipticity of an object and are likely to affect other morphological quantities in a similar way. Hence, it was obvious to introduce a set of basis functions based on the Sérsic profile (Ngan et al. 2009), called “sérsiclets”. As these basis functions explicitly account for the steepness of radial profiles, they are highly flexible and seem to be promising candidates to provide a method for describing the huge variety of different galaxy morphologies.

This article is organised as follows. We define sérsiclet basis functions in Sect. 2. Section 3 presents systematic tests of sérsiclets, working out their reliability and limitations. We investigate the performance of sérsiclets in an application to artificial weak-lensing data in Sect. 4. In Sect. 5 we discuss the potential of enhancing the Sérsic profile by higher-order Taylor expansions and briefly investigate the orthonormalisations of such light profiles. We conclude in Sect. 6. Further details are given in the appendices. Appendix A contains the proof that Sérsic profiles are first-order Taylor expansions. Appendix B provides the analytic derivation of the sérsiclet basis functions. Finally, we explain in Appendix C how to fit sérsiclet models to imaging data.

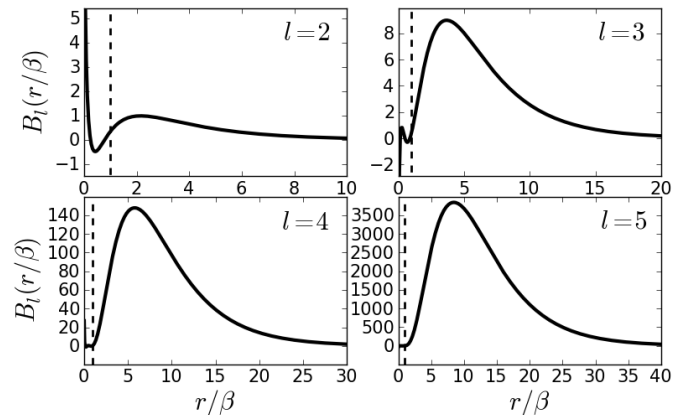


Figure 1. Radial basis functions if orthonormalised on the integration interval $r \in [0, \beta]$ using a Sérsic profile with index $n_S = 2$ as weight function (Ngan et al. 2009). The vertical dashed lines indicate $r = \beta$, where the orthonormalisation interval ends. The Sérsic profile is not able to suppress the polynomials outside the orthonormalisation interval.

2 POLAR SÉRSICLETS

We briefly comment on a prior attempt to introduce sérsiclets before we then give our definition.

2.1 The first attempt to introduce sérsiclets

Given the aforementioned problems of shapelets, it was obvious to orthonormalise the Sérsic profile. Moreover, this choice is “natural” because the Sérsic profile is the first-order Taylor expansion of any real light profile (cf. Appendix A1). This is likely to remove the strong biases of shapelets. The resulting basis functions are called sérsiclets and were first investigated by Ngan et al. (2009).

However, Ngan et al. (2009) faced a severe problem with sérsiclets. In a simple test case, Ngan et al. (2009) observed that the polar sérsiclets were incapable of fitting a given object. Even when increasing the number of basis functions used for the decomposition, the model did not converge to the given image data. This directly implies that the basis functions constructed by Ngan et al. (2009) are not complete. We found out that this problem originates from the fact that Ngan et al. (2009) orthonormalised their basis functions out to one half-light radius – not on the interval $r \in [0, \infty[$ – but then extended their basis functions beyond this range. Figure 1 shows what happens in this case. In the inner region, the basis functions may be orthonormal, but for larger radii the leading order monomial in the basis functions dominates over the Sérsic profile. This creates an artificial bump outside the region of orthonormality, which appears in all radial modes of order $l > 0$ and becomes the dominant feature. Consequently, these basis functions lose their linear independence, which explains the non-convergence observed by Ngan et al. (2009).

In order to solve this problem, they suggested to discard all modes with azimuthal “quantum number” $m \neq 0$, i.e., all mode with azimuthal structure, and only maintain the radial modes. While this approach may be viable for weak-lensing applications, where azimuthal structures are rarely visible, it does not solve the actual problem, which is the extension

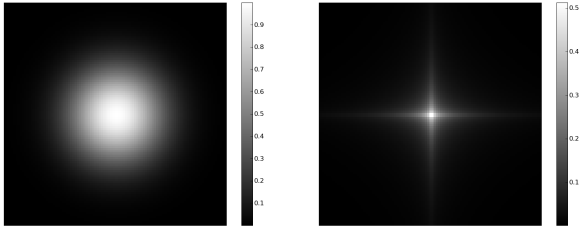


Figure 2. Cartesian ground state using Gaussian profile (left panel) and Sérsic profile with index $n_S = 2$ (right panel). Unless we employ the Gaussian profile, the Cartesian weight function is not spherically symmetric.

beyond the orthonormalisation interval. Moreover, the resulting basis functions may still represent an expansion into radial modes, but it is not only radial but also azimuthal structure of galaxies that is interesting, e.g., in morphological classification. In fact, it is the ability to describe azimuthal structure in a (theoretically) well defined way that makes basis-function expansions of galaxy morphologies such a compelling approach. Consequently, Jiménez-Teja & Benítez (2011) criticised that this implementation of sérsiclets is incapable of describing irregular galaxies.

2.2 Definition of polar sérsiclets

We now define the sérsiclet basis functions. In the case of shapelets, we can define both Cartesian and polar shapelets due to the mathematical features of the Gaussian weight function. However, for general Sérsic profiles, we cannot meaningfully define Cartesian basis functions because the ground states hardly resemble any known galaxy morphology, as is shown in Fig. 2. Therefore, we have to introduce sérsiclets as polar basis functions.

The crucial idea to overcome the problems faced by Ngan et al. (2009) is to realise that we *cannot* expect a galaxy’s structure being well captured within one half-light radius. For instances, disc galaxies may exhibit spiral-arm patterns in their outskirts. Therefore, we require orthonormality on the full interval $r \in [0, \infty[$. Apart from solving the problems reported by Ngan et al. (2009), this also has the advantage that the orthonormal polynomials exist analytically. The sérsiclet basis functions are derived in Appendix B and are given by

$$R_l(r) \propto L_l^{2n_S-1} \left[b(r/\beta)^{1/n_S} \right] \exp \left[-\frac{b}{2} (r/\beta)^{1/n_S} \right], \quad (1)$$

where the normalisation factor is also derived in Appendix B. Apart from the linear expansion coefficients, sérsiclets have the following nonlinear model parameters:

- The maximum order N_{\max} .
- The Sérsic index n_S .
- The scale radius β .
- The centroid position \vec{x}_0 , which enters via $r = |\vec{x} - \vec{x}_0|$.
- The complex ellipticity ϵ , which enters via a shear transformation (e.g. Bartelmann & Schneider 2001) thereby affecting r .¹

¹ It is advantageous to use the real and imaginary parts of the complex ellipticity as model parameters, rather than orientation

The coefficient b is defined by (Graham & Driver 2005)

$$\Gamma(2n_S) = 2\gamma(2n_S, b), \quad (2)$$

where Γ and γ denote the complete and incomplete gamma functions. We explain in Appendix C how to fit these model parameters for given imaging data. In the case of $n_S = 0.5$ and $b = 1$ the polar sérsiclets reduce to the special case of polar shapelets.² Furthermore, for $n_S = 1$ and $b = 1$, we get a set of basis function that could be called “disclets”, since they have an exponential profile as weight function. Similarly, we could define “deVaucouleurlets”. All these sets are special cases of Eq. (1). Finally, we emphasise that when fitting a sérsiclet model, we always also fit a Sérsic model, which is the ground state of the sérsiclets. Figure 3 displays an example of sérsiclet basis functions.

2.3 Interpretation of the Sérsic index

In the case of sérsiclet basis functions, the Sérsic index n_S changes its interpretation. First, n_S regulates the steepness of the weight function, which is a normal Sérsic profile. Second, via the steepness of the weight function, n_S also regulates the spatial scale on which the associated Laguerre polynomials oscillate. In simple words, there is a fixed relation between steepness of the weight function and oscillation scale of the polynomials. However, real morphologies do not necessarily obey such a relation. For instances, the steepness of the bulge is not related to the positions of spiral arms or star-forming regions. In practice, this can lead to modelling problems, if the steepness of the profile and the range of oscillation scales required for a faithful description of a given galaxy morphology do not match.

3 TESTING SÉRSICLETS

Before we can apply sérsiclets to scientific questions, we need to investigate the performance and fidelity of sérsiclets.

3.1 Completeness

First, we need to test the completeness of sérsiclets in order to proof that we indeed overcome the problems reported by Ngan et al. (2009). We decompose three real galaxy images from the Sloan Digital Sky Survey into sérsiclets with increasing maximum order. If our basis functions were not linearly independent, completeness would break down and the χ^2 -values would not decrease with increasing maximum order as in the case of Ngan et al. (2009). Figure 4 shows the results. First and foremost, the residuals of sérsiclets are decreasing with increasing maximum order, i.e., we indeed set up a set of basis functions that are linearly independent. Furthermore, it is interesting to compare the residuals of sérsiclets with those of circular shapelets. In the

angle and axis ratio. Using the orientation angle as parameter would cause severe problems with convergence in the case of nearly spherical objects.

² Note that the polar functions defined by Massey & Réfrégier (2005) are not orthogonal. A correct functional form of polar shapelets is derived in Appendix B.

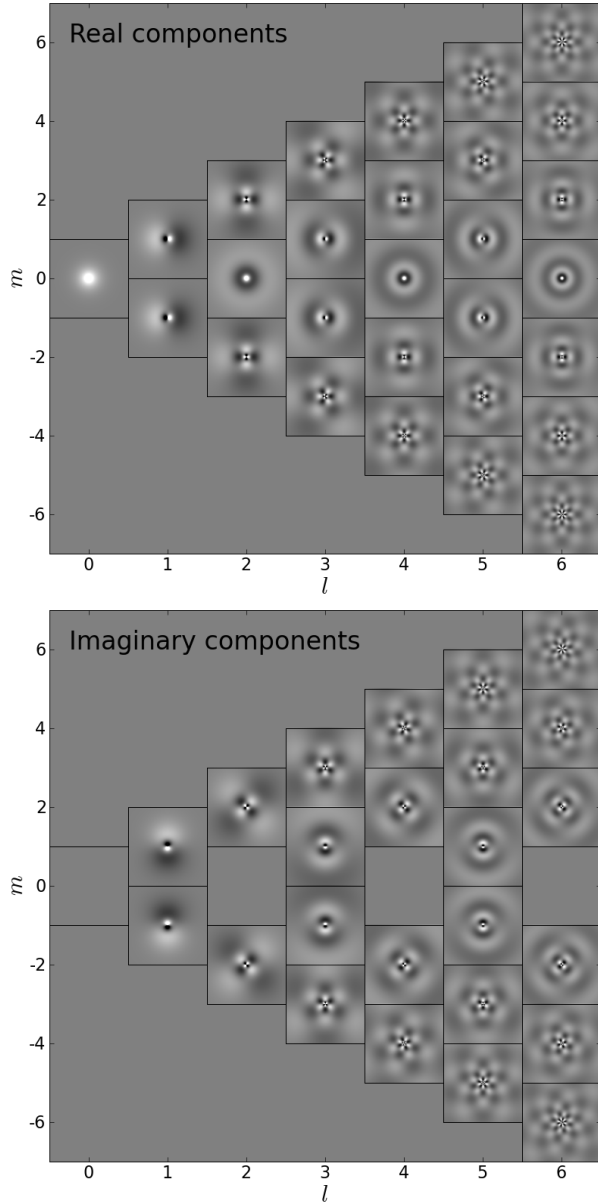


Figure 3. Polar sérsiclet basis functions with $n_S = 1$, $b = 1$, and $\epsilon = 0$. The real components of the complex-valued basis functions are shown in the top panel, the imaginary components in the bottom panel. The basis functions with $m = 0$ are wholly real. We note that the polar basis functions exhibit lots of substructure in the central region. Moreover, these central substructures become very small with increasing radial order l .

case of the spiral galaxy, sérsiclets yield residuals comparable to shapelets. This is not surprising, because shapelets excel in modelling extended objects with lots of substructure, such as a face-on spiral galaxy. However, in the case of the edge-on disc and the elliptical galaxy, the χ^2 -values of sérsiclets are substantially lower. Evidently, sérsiclets outperform shapelets in modelling galaxies of these types, as expected from the steep light profiles.

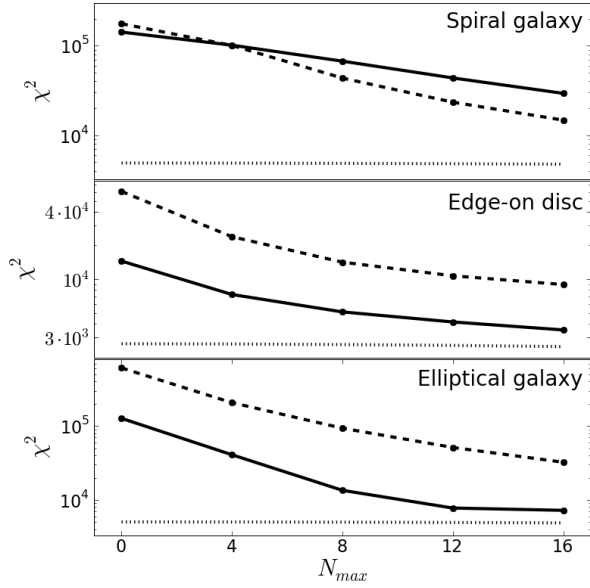


Figure 4. Dependence of χ^2 of sérsiclet decomposition (solid lines) and shapelet decompositions (dashed lines) on maximum order, N_{\max} , for the spiral galaxy, the edge-on disc, and the elliptical galaxy shown in Fig. 5. For each example, we also show the number of pixels as a horizontal dotted line.

3.2 Image decompositions

We have seen in the previous section that sérsiclet decompositions produce substantially lower residuals than (circular) shapelet decompositions when it comes to modelling galaxies that exhibit steep profiles, such as elliptical galaxies or edge-on discs. However, we still have to check whether sérsiclets indeed overcome the ring-like artefacts produced by shapelets.

Figure 5 compares the best-fitting models and residuals of (circular) shapelets and (elliptical) sérsiclets using $N_{\max} = 8$ for the three test galaxies. As expected from the similar χ^2 -values, in the case of the spiral galaxy, both shapelets and sérsiclets perform well in modelling the spiral-arm patterns. Sérsiclets fit the central region better than shapelets, whereas shapelets tend to describe the outskirts better. As expected from a sérsiclet model with $n_S > 0.5$, the polynomial oscillations appear on smaller scales than for the shapelet model with $n_S = 0.5$. In the case of the edge-on disc, sérsiclets are clearly superior. First, the ring-like artefacts of shapelets are gone. Second, the intrinsic ellipticity of the sérsiclet model allows the basis functions to also describe the outermost regions of the disc, whereas these regions go almost unfitted by circular shapelets. In the case of the elliptical galaxy, the ring-like artefacts are very prominent in the shapelet residuals. Conversely, the sérsiclet residuals do not exhibit any artefacts of this kind, i.e., the steepness of the light profile is indeed described properly.

3.3 Orthonormality and sampling

Let Σ denote the pixel covariance matrix of the noise in the imaging data and X the design matrix (see Appendix C1). In order to get the maximum-likelihood estimate of the ex-

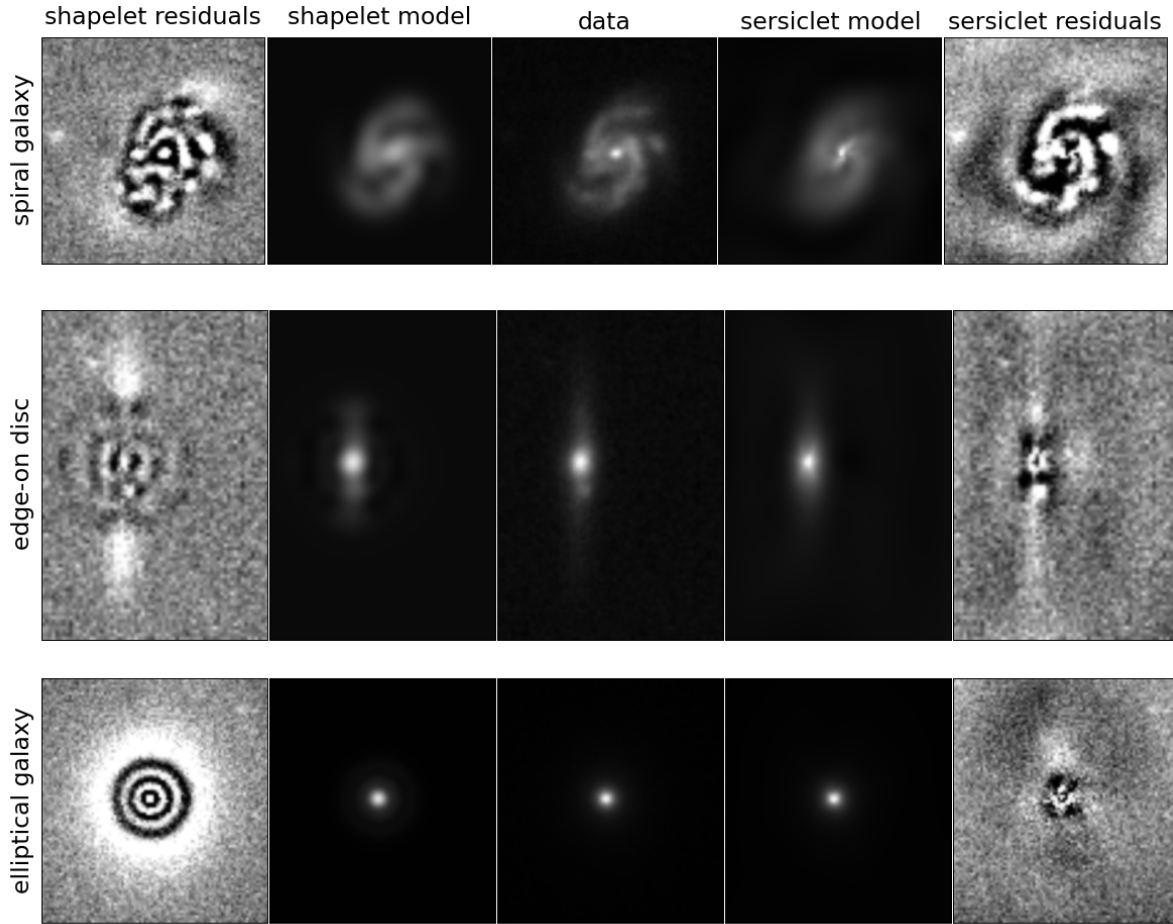


Figure 5. Models and residual maps resulting from sérsiclets and shapelets for the spiral galaxy (top row), the edge-on disc (central row), and the elliptical galaxy (bottom row). All models used $N_{\max} = 8$. For the sake of visualisation, the colour code of the model and data maps is nonlinear and ranges from -4.5σ to the maximum value. The colour code of the residual maps is linear and ranges from -4.5σ to $+4.5\sigma$, where σ denotes the standard deviation of the background noise. The *peak* significance of the imaging data is 132σ for the spiral galaxy, 101σ for the edge-on disc, and 610σ for the elliptical galaxy.

pansion coefficients from Eq. (C3), the matrix $X^T \cdot \Sigma^{-1} \cdot X$ – or $X^T \cdot X$ for uncorrelated pixel noise – needs to be invertible. If it were not for pixellation, finite image grids, and the PSF, $X^T \cdot X$ should be an identity matrix due to the orthonormality of the basis functions. We now investigate the orthonormality of sérsiclets in two tests.

First, we compare the orthonormality of *polar* shapelets (sérsiclets with $n_S = 0.5$ and $b = 1$) and *Cartesian* shapelets of Melchior et al. (2007). We sample polar and Cartesian shapelets of constant scale radius $\beta = 5$ on pixel grids of sizes 50×50 , 100×100 , and 500×500 and compute the determinant of $X^T \cdot X$ for maximum orders $0 \leq N_{\max} \leq 16$, where $\det(X^T \cdot X) < 1$ indicates a violation of orthonormality. Figure 6 shows the results of this test. In the case of the 50×50 grid (panel (a)) both Cartesian and polar shapelets suffer from non-orthonormality for increasing N_{\max} .³ This problem can be caused either by boundary truncation or undersampling of higher-order modes (with rapidly oscillat-

ing polynomials). Therefore, in panel (b) we increase the pixel grid from 50×50 to 100×100 . The non-orthonormality of Cartesian shapelets is now cured, i.e., it has indeed been caused by boundary truncation. However, polar shapelets still exhibit non-orthonormality. Therefore, in panel (c) we increase the pixel grid again now from 100×100 to 500×500 . The behaviour of polar shapelets is unchanged, i.e., the non-orthonormality is not caused by boundary truncation. In order to demonstrate that the non-orthonormality is caused by undersampling, we increase in panel (d) the object size from $\beta = 5$ to $\beta = 25$ while keeping the 500×500 pixel grid. The non-orthonormality of polar shapelets is now almost cured, which verifies that this was an undersampling effect. Evidently, undersampling has a larger impact on polar shapelets than on Cartesian shapelets. The reason is that polar basis functions exhibit most of their structure in the central region (cf. Fig. 3) and therefore suffer strongly from pixellation. Loosely speaking, *polar* basis functions do not appreciate being sampled on a *Cartesian* pixel grid.

³ In particular, for polar shapelets and $N_{\max} \geq 8$ the determinant of $X^T \cdot X$ is zero, i.e., $X^T \cdot X$ is not invertible and the estimator of the expansion coefficients (Eq. (C3)) breaks down.

Second, having attested problems of polar shapelets with orthonormality due to undersampling, we now investigate the orthonormality of (polar) sérsiclets in general. We

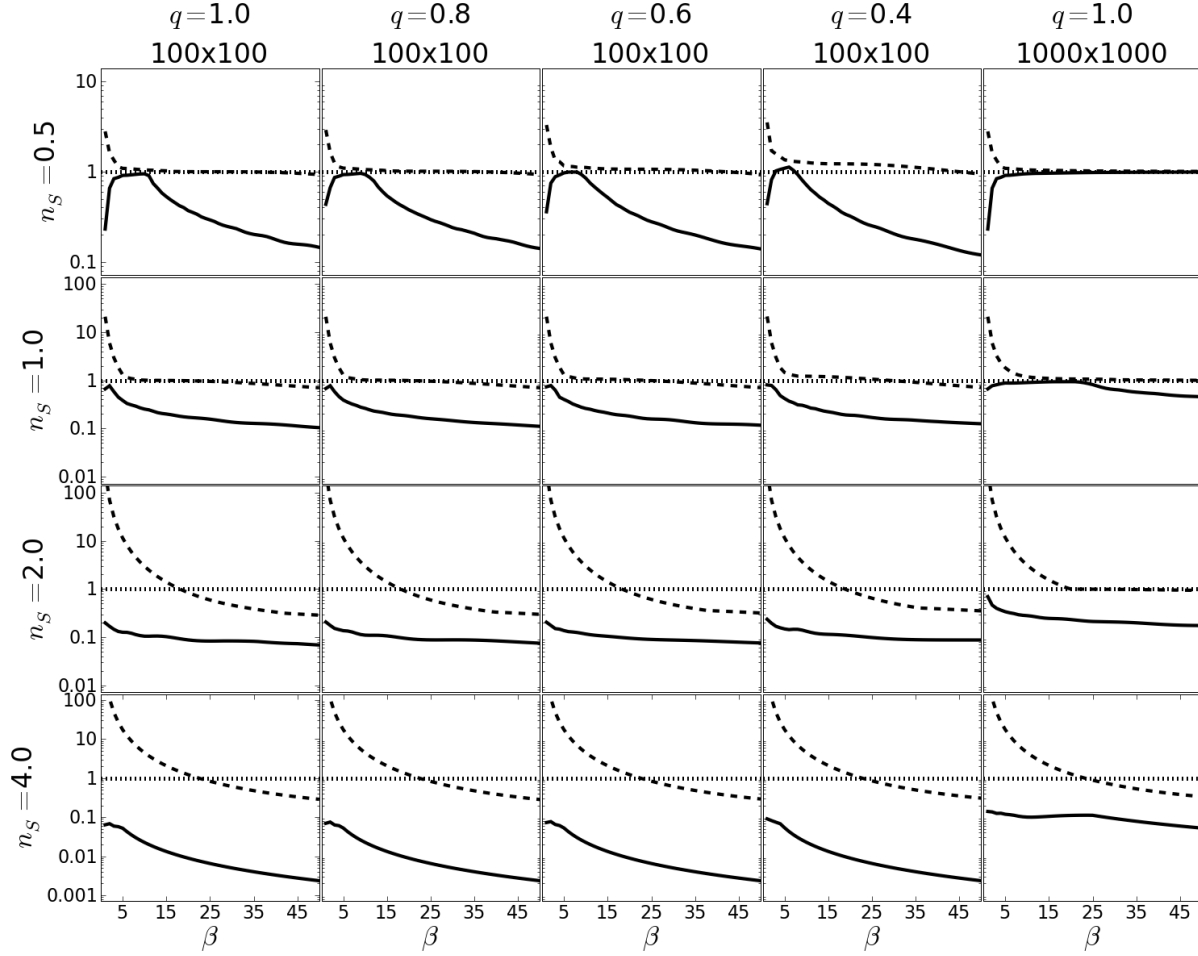


Figure 7. Smallest (solid line) and largest (dashed line) diagonal elements of matrix $X^T \cdot X$ as a function of β at $N_{\max} = 12$. Deviation from unity (dotted line) indicates the loss of orthonormality. The image size was 100×100 pixels (left columns) and 1000×1000 pixels (right column). We used $b = 2 \log 3$, such that at one scale radius the weight function drops to one third of its central value.

compare the value of the largest and smallest diagonal element of $X^T \cdot X$, respectively, repeating the same test as Berry et al. (2004) did for shapelets. We evaluate sérsiclet models of maximum order $N_{\max} = 12$, Sérsic indices $n_S = 0.5, 1, 2, 4$ and axis ratios $q = 1, 0.8, 0.6, 0.4$ on a 100×100 pixel grid for varying scale radii β . There is no PSF in this test. Figure 7 shows test results. For the moment, we only consider the first row in Fig. 7, which corresponds to polar shapelets. The results agree with Fig. 6, revealing undersampling effects for small β and boundary truncation for large β (cf. Melchior et al. 2007, and discussion therein). Furthermore, we can see that the axis ratio has only a mild impact on the orthonormality. However, inspecting the other rows corresponding to steeper profiles ($n_S = 1, 2, 4$), Fig. 7 reveals serious violations of orthonormality. Obviously, for $n_S \geq 1$ the undersampling regime is not overcome before the boundary effects set in. This is confirmed by the right-most column in Fig. 7, which used an enlarged pixel grid while keeping the resolution (scale radius β) constant. In this case, sérsiclets with $n_S = 1$ exhibit decent orthonormality on this larger grid, while the cases with $n_S > 1$ still do not reach an acceptable level of orthonormality. The reason for this peculiar behaviour is the argument $b(r/\beta)^{1/n_S}$ of the associated

Laguerre polynomials in Eq. (1). It implies that the polynomials are only slowly varying with r for large values of n_S . Consequently, polar sérsiclets have a serious problem with orthonormality, especially for large Sérsic indices.

What is the impact of undersampling? If $\det(X^T \cdot X)$ is too close to zero, numerical inaccuracies will dominate its inversion and the estimate of the expansion coefficients (Eq. (C3)) will catch up random errors. Consequently, this increases the uncertainty in the model parameters and may even lead to completely random parameter values.

The impact of undersampling could be alleviated by sampling the model several times within each pixel. In the limit of infinitely fine sampling this amounts to a convolution of the model with the pixel-response function. As the undersampling problem stems from a key feature of the employed sérsiclet model, namely rapid polynomial oscillations, an oversampled model may better approximate the image data. However, the information about the galaxy morphology contained in the expansion coefficients has been lost and is not restored by oversampling. Instead, excessive oversampling generates artificial information that compromises the model parameters. As we require meaningful information from the expansion coefficients, we will not further pursue

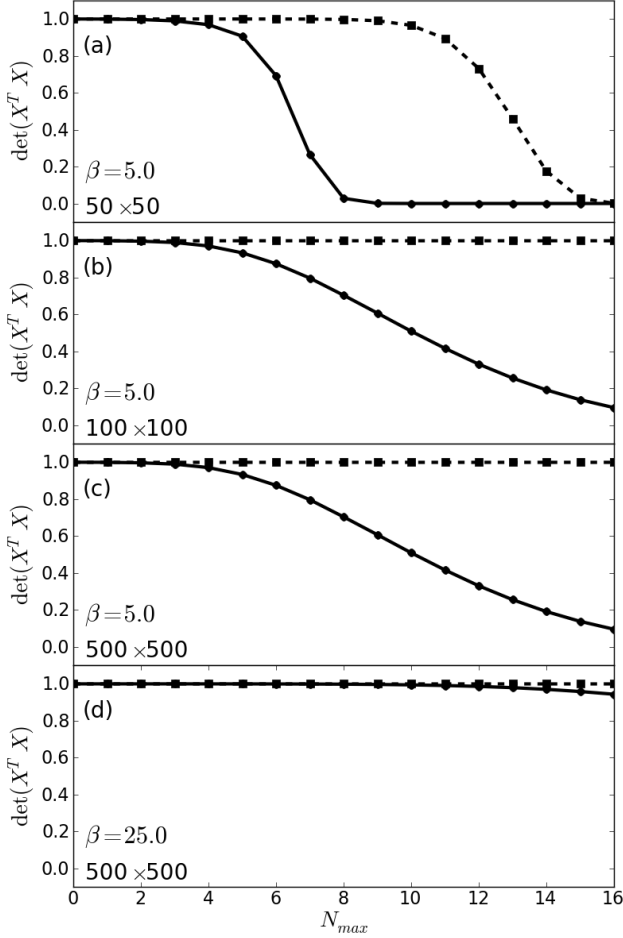


Figure 6. Determinant of $X^T \cdot X$ for Cartesian (dashed lines with squares) and polar (solid lines with dots) shapelets for increasing maximum order N_{\max} , different scale radii β and grid sizes. Panel a: At large N_{\max} both Cartesian and polar shapelets deviate from $\det(X^T \cdot X) = 1$. Panel b: Cartesian shapelets maintain $\det(X^T \cdot X) = 1$ for all N_{\max} , proving that boundary effects are now negligible. Panel c: Polar shapelets still differ from $\det(X^T \cdot X) = 1$ at large N_{\max} on this enlarged grid, i.e., this is not a boundary effect. Panel d: Polar shapelets now also maintain $\det(X^T \cdot X) = 1$, i.e., the remaining effect was due to undersampling.

this approach. If one wants to employ this approach, one has to bear in mind, that the additional convolution will lead to covariances among the coefficients and therefore render the fitting procedure more complicated.

3.4 Analogy to Nyquist frequency

In order to avoid the undersampling problem in practice, e.g., in morphological classification, we want to derive a lower limit to the scale radius β of a sérsiclet model. This limit is given by comparing the pixel size to the scale on which the radial components of sérsiclets – essentially the Laguerre polynomials – vary. In fact, this is an analogy to the Nyquist frequency in the case of Fourier transform.

The key to set this lower limit is to identify the shortest scale on which a Laguerre polynomial varies. This scale can be inferred from the roots of the Laguerre polynomial.

N_{\max}	$n_S = 0.5$	$n_S = 1.0$	$n_S = 2.0$	$n_S = 3.0$	$n_S = 4.0$
1	0.8165	0.8333	0.8403	0.8424	0.8435
2	1.0668	1.3145	1.7599	2.2042	2.6658
3	0.3256	1.7810	2.9324	4.3311	6.0286
4	1.4377	2.2423	4.3625	7.3782	11.537
5	1.5904	2.7011	6.0513	11.499	19.888
6	1.7296	3.1586	7.9993	16.848	31.873
7	1.8584	3.6151	10.207	23.577	48.375
8	1.9787	4.0712	12.674	31.841	70.372
9	2.0921	4.5268	15.400	41.792	98.931
10	2.1996	4.9821	18.386	53.584	135.22
11	2.3021	5.4373	21.632	67.371	180.49
12	2.4002	5.8922	25.137	83.305	236.08
13	2.4944	6.3471	28.902	101.54	303.46
14	2.5853	6.8018	32.926	122.23	384.13
15	2.6730	7.2565	37.210	145.53	479.75
16	2.7579	7.7110	41.754	171.59	592.02
17	2.8403	8.1656	46.557	200.57	722.76
18	2.9204	8.6201	51.620	232.61	873.87
19	2.9983	9.0745	56.943	267.88	1047.4
20	3.0742	9.5289	62.525	306.52	1245.3

Table 1. Lower limits of scale radii β in units of pixels for different maximum radial orders N_{\max} according to Eq. (4). Here we used $b = 2n_S - 1/3$.

An associated Laguerre polynomial $L_l^k(x)$ of order l has l real-valued, positive roots within the interval $(0, l + k + (l - 1)\sqrt{l + k}]$. The smallest scale that can be resolved by this polynomial is given by the distance between $x = 0$ (the peak of the radial component) and the first root $x_1 > 0$. Unfortunately, the roots of associated Laguerre polynomials are not known analytically, so the first root x_1 has to be inferred numerically. As the argument of the associated Laguerre polynomial is $x = b(r/\beta)^{1/n_S}$, given x_1 , we can infer the radius of the first root to be $r_1 = \beta(x_1/b)^{n_S}$. Hence, the distance between $r = 0$ and the first root is given by

$$\Delta r = r_1 - 0 = r_1 = \beta(x_1/b)^{n_S}. \quad (3)$$

This scale Δr should be well resolved by the pixel grid in order to avoid undersampling. An optimistic lower limit is $\Delta r = 1$, i.e., the radial component drops from its central peak to its first root within a single pixel. Setting $\Delta r = 1$ and solving for the minimal β , we obtain,

$$\beta \geq \beta_{\min} = (b/x_1)^{n_S}, \quad (4)$$

where β and hence β_{\min} are given in units of pixels. Table 1 provides values of β_{\min} for some realistic values of n_S and maximum polynomial order $N_{\max} = l$. Considering this table, we also have to keep in mind that the image grid has to be large enough such that several scale radii fit into it. Evidently, as n_S increases, the limit becomes larger and larger. This can also be inferred qualitatively from Fig. 7, but Eq. (4) provides a quantitative result. Obviously, for $n_S \geq 2$ the lower limit becomes extraordinarily large. In particular, $n_S = 4$ would require an extremely well resolved object with radius of several thousand pixels.

In the case of shapelets, it is standard practice to choose a maximum order N_{\max} for a decomposition according to signal-to-noise ratio and resolution. For sérsiclets, the resolution constraint plays a much more important role and restricts models with large n_S to low N_{\max} , with which com-

Set	g_1	g_2
0007	0.0005405	0.0069236
0026	-0.0527875	-0.0090224
0035	0.0166067	-0.0045223
0048	0.0708862	-0.0377040
0056	0.0325078	0.0978346
0091	-0.0246346	-0.0488837
0126	0.0170977	-0.1383142
0135	0.0596913	0.0416342
0268	-0.0653126	-0.0883511
0281	-0.0431769	0.0462176

Table 2. Data sets chosen from the GREAT08 sample and their complex shears $g = g_1 + ig_2$.

plicated morphological features could receive improper description. As elliptical galaxies rarely exhibit such features though, this restriction may not be overly problematic.

4 APPLICATION TO WEAK-LENSING DATA

Given the fact that shapelets were also intended for shear measurements in weak-gravitational lensing (e.g., Réfrégier & Bacon 2003; Chang et al. 2004), we now study the potential of sérsiclets in this field of research. From the simulated GREAT08 data (Bridle et al. 2009) we selected ten images with artificial galaxies, whose shear values are given in Table 2.⁴ Every set contains 10,000 objects sampled on a 40×40 pixel grid. Within such a set the applied shear is constant and the aim is to retrieve its value. Furthermore, all objects have been convolved with a PSF that is a Moffat profile with FWHM = 2.85, $\beta = 3.5$, and intrinsic ellipticity $\epsilon = 0.019 - 0.007i$ (cf. Bridle et al. 2010).

We decompose all objects into sérsiclets with maximum orders $N_{\max} = 0, 2, 4, 6$, taking into account the PSF by forward modelling. For each set, the shear is estimated via the mean ellipticity $\hat{\epsilon}$ from the 10,000 artificial galaxies via the ellipticity parameter of the sérsiclet model, which theoretically provides an unbiased estimator of the gravitational shear (cf. Bartelmann & Schneider 2001). Figure 8 shows the test results as input vs. estimated shear. The goodness of the shear estimates is parametrised by a straight-line model

$$f(x) = a + bx. \quad (5)$$

A perfect shear estimator yields $a = 0$ and $b = 1$. If a real shear estimator yields an offset $a \neq 0$, i.e., a shear is detected although the input shear was zero, this typically implies that the PSF is not properly corrected for. If $b < 1$, the true shears are underestimated.

Given the test results shown in Fig. 8, the sérsiclets perform best for $N_{\max} = 0$, where the slope b is consistent with 1 (at a fairly large offset a). This is not surprising, because for $N_{\max} = 0$ sérsiclets reduce to pure Sérsic profiles, which were used to simulate this subset of the GREAT08 data.⁵

⁴ This restriction on only ten sets was necessary, because analysing the whole GREAT08 data set would have been too time-consuming.

⁵ The data sets were taken from the Great08 RealNoiseKnown branch, for which the galaxies are modeled as either of bulge or

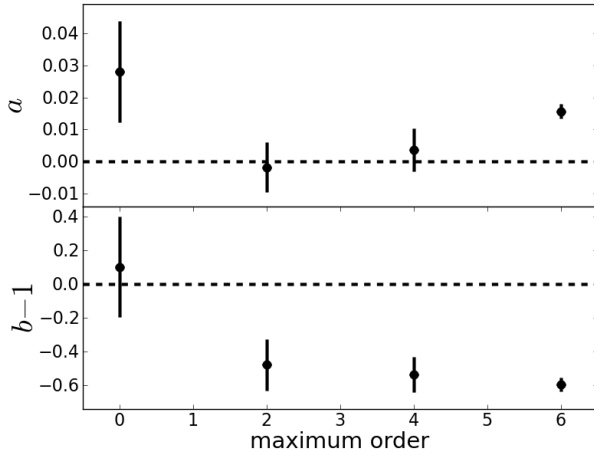


Figure 8. Offset a (top) and deviation from unity slope $b - 1$ (bottom) of GREAT08 data sets given in Table 2 for different maximum orders, N_{\max} , of sérsiclet decomposition. Horizontal dashed lines indicate the ideal case of $a = 0$ and $b = 1$. Errors of a and b were estimated by bootstrap fitting of $f(x) = a + bx$ to the estimated and input shear values.

However, the real lesson from Fig. 8 is that for $N_{\max} > 0$ the slopes are significantly below 1, i.e., the shear is significantly underestimated. The higher-order sérsiclet modes, which should account for any deviation the actual galaxy shape exhibits with respect to the axisymmetric Sérsic profile, do more harm than good as they become increasingly prone to undersampling. Low resolution is a generic feature of weak-lensing data, i.e., shear estimates based on sérsiclet decompositions always suffer from substantial undersampling effects. Oversampling of the model within each pixel could cure this, but is – at least in our implementation – computationally infeasible. Finally, we note that we observed a bias in the shear estimates based on Sérsiclets. The first component of the shear is systematically overestimated whereas the second component is systematically underestimated. We do not yet understand the precise origin of this bias but we may speculate that this is a pixellation effect (cf. Sect. 5.3 of Massey et al. 2007).

5 OUTLOOK: ORTHONORMALISING HIGHER-ORDER TAYLOR EXPANSIONS

As discussed in Appendix A, the Sérsic profile is the first-order Taylor expansion of any light profile. This naturally leads us to the expectation that with improving imaging quality the Sérsic profile will not be a good match anymore, because it is “only” a *first-order* expansion. Consequently, an obvious strategy to enhance the Sérsic profile is to allow for higher orders in the Taylor expansion of Eq. (A2). Such higher-order radial profiles then can also be orthonormalised in order to describe azimuthal structures. This approach appears to be very promising for investigations of galaxy morphologies, e.g., in the context of classification. However, it

disc type, i.e. having Sérsic index of $n_S = 1$ or $n_S = 4$, respectively.

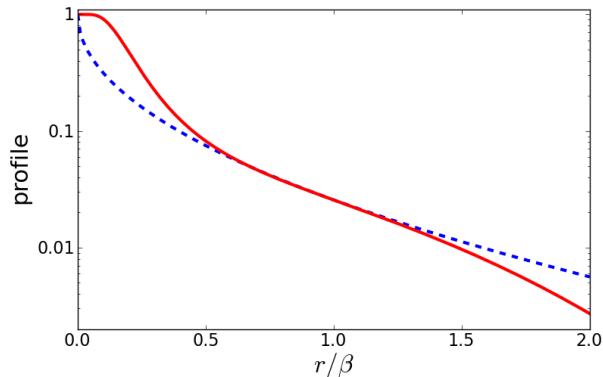


Figure 9. Comparing a Sérsic profile with $n_S = 2$ (blue dashed line) to a third-order profile with $B = 1/n_S = 0.5$, $C = 0.1$ and $D = 0.25$ (red solid line).

introduces further nonlinear model parameters which renders it inappropriate for investigations of weak lensing where notoriously little data is available to constrain the model.

5.1 Third-order profiles

As explained in Appendix A2, the next useful higher-order expansion which exhibits the correct boundary behaviour beyond the Sérsic profile is a third-order expansion,

$$p(r) \approx \exp \left[-e^{A+B \log(r/\beta)+C \log^2(r/\beta)+D \log^3(r/\beta)} \right], \quad (6)$$

where $D > 0$ and A , B , and C are arbitrary. Figure 9 shows an example of such a third-order profile in comparison to a normal Sérsic profile. Evidently, the third-order profile can overcome two essential problems of pure Sérsic profiles, since it (a) can exhibit a central cusp, which is also observed in real galaxies, and, (b) approaches zero for increasing radii faster than the pure Sérsic profile. Therefore, we may speculate that such higher-order Taylor expansions could provide a reasonable generalisation, if deviations from the normal Sérsic profile are observed while azimuthal structures are still absent. For instances, this may help to describe the light profiles of elliptical galaxies or unbarred S0 galaxies.

In Fig. 10 we compare the performances of the third-order profile and the Sérsic profile by fitting an elliptical galaxy from the SDSS database. Clearly, the residual map of the third-order profile is almost perfectly random noise whereas the residual map of the Sérsic profile reveals systematic mismodelling. Correspondingly, the ratio of χ^2 -values of the third-order profile over Sérsic fit is $\chi_3^2/\chi_S^2 \approx 0.48$. In fact, the third-order profile fits the data so well that we should ensure that it is not an overfit. For this purpose, Fig. 11 displays the distributions of normalised residuals for both models in comparison to the unit Gaussian (e.g. see Andrae et al. 2010c). Evidently, the normalised residuals of the Sérsic profile have a broader distribution than the unit Gaussian which is indicative of underfitting the data. The normalised residuals of the third-order profile are closer to the unit Gaussian, i.e., they are closer to the truth. However, their distribution does *not* peak sharper than the unit Gaussian, i.e., the third-order profile does not overfit the data.

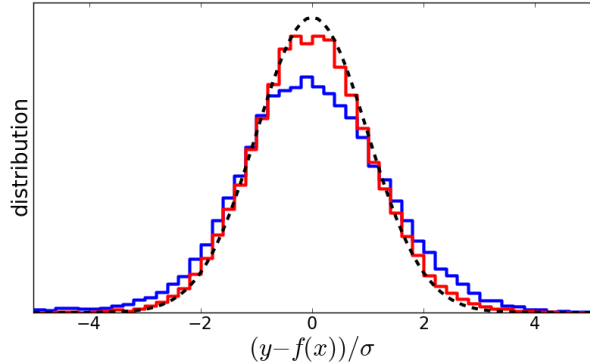


Figure 11. Model comparison via distributions of normalised residuals. The blue histogram shows the distribution of normalised residuals from the Sérsic fit. The red histogram are the normalised residuals from the third-order profile. The black dashed line is a unit Gaussian.

5.2 Numerical orthonormalisation

Third-order profiles such as Eq. (6) can be orthonormalised, too. Unfortunately, it is not possible to do this orthonormalisation analytically.⁶ Therefore, the orthonormalisation has to be performed numerically. We start with the radial monomials ($r^0, r^1, r^2, r^3, \dots$) which are linearly independent but not orthonormal. Using the definition of the scalar product according to Eq. (B1) and Dirac notation, we first normalise the ground state,

$$|0\rangle = \frac{|r^0\rangle}{\langle r^0|r^0\rangle}. \quad (7)$$

Second, we compute the first-order state

$$|1\rangle = (\hat{r} - \langle 0|\hat{r}|0\rangle) |0\rangle, \quad (8)$$

which is then also normalised such that $\langle 1|1\rangle = 1$. Here, we used the following definition,

$$\langle k|\hat{r}|l\rangle = \int_0^\infty dr r B_k(r) r B_l(r), \quad (9)$$

where B_l denotes the radial basis function of order l . The basis functions of order $l \geq 2$ are then computed using the three-term recurrence relation

$$|l\rangle = (\hat{r} - \langle l-1|\hat{r}|l-1\rangle) |l-1\rangle - \langle l-1|\hat{r}|l-2\rangle |l-2\rangle. \quad (10)$$

This requires less numerical integrations than the brute-force Gram-Schmidt algorithm. Hence, it is faster and numerically more stable than the Gram-Schmidt algorithm.

5.3 Revisiting the problems of sérsiclets

The conceptual problem of sérsiclets was the postulated relation of steepness of the weight function and scale of polynomial oscillations that is not obeyed by real galaxies. This fixed relation is loosened by the third-order profiles. Of course, the Sérsic index – or rather $B = \frac{1}{n_S}$ – still has an influence on the oscillation scale of the radial polynomials. However, now there are two further model parameters C and

⁶ The reason is that the substitution in Appendix B is not bijective anymore.

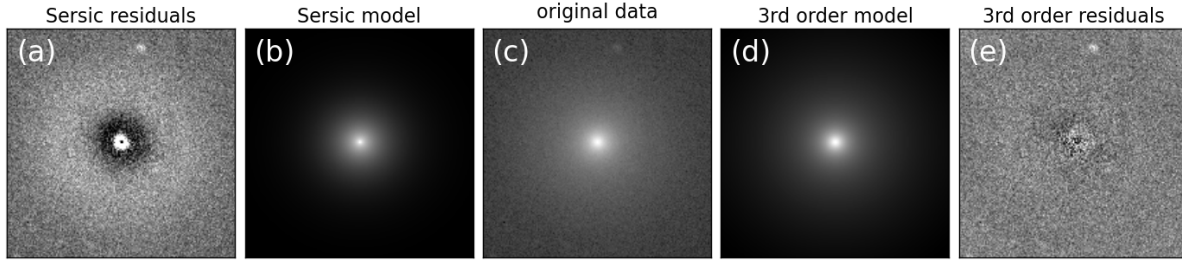


Figure 10. Fitting Sérsic and third-order profile to an elliptical galaxy. The panels denote residual map of Sérsic fit (a), Sérsic model (b), original data (c), best-fitting third-order profile (d), and residual map from third-order profile (e). Panels, b, c, and d have identical scaling. The residual maps (panels a and e) both use plot ranges from -5σ to 5σ .

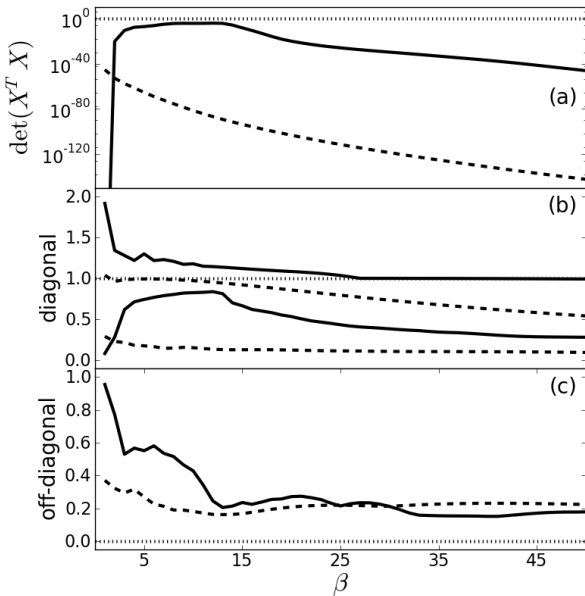


Figure 12. Undersampling test for third-order profiles. We compare basis sets of the Sérsic (dashed lines) and third-order profile (solid lines) shown in Fig. 9. The test is performed on a 100×100 pixel grid and the weight function has no intrinsic ellipticity. In contrast to Fig. 7, we have chosen $b = 4 - 1/3$ in this case. Panel a: Determinant of coefficient covariance matrix of $X^T \cdot X$ which should be 1. Panel b: Largest and smallest diagonal elements of $X^T \cdot X$ which should be 1. Panel c: Largest absolute value of off-diagonal elements of $X^T \cdot X$ which should be 0.

D which also influence the polynomials. Consequently, basis functions based on third-order profiles are more flexible and do not impose such a rigid relation as sérsiclets do.

The practical problem of sérsiclets was undersampling, in particular for Sérsic indices $n_S \geq 1$. In fact, Fig. 9 already suggests that third-order profiles can overcome this problem because they can exhibit central cusps instead of peaks. Therefore, the weights are not as highly concentrated and the polynomials may not oscillate as rapidly. We demonstrate this by repeating the orthonormality test of Fig. 7 for the third-order profile with parameters given in Fig. 9 and its set of basis functions. Figure 12 shows the test results. In direct comparison to sérsiclets with $n_S = \frac{1}{B} = 2$, the orthonormalised third-order profile indeed suffers less strongly from undersampling, which is most obvious for the determi-

nant of $X^T \cdot X$. In particular, there is a regime $5 \leq \beta \leq 15$ where undersampling is overcome and boundary truncation has not yet set in. Such a regime does not exist for the corresponding set of sérsiclets shown here. Consequently, third-order profile can indeed overcome the undersampling problem of sérsiclets. Nevertheless, there are parameter choices for third-order profiles where the undersampling problem is as bad as for sérsiclets, e.g., when $C = D = 0$ and the third-order profile reduces to a Sérsic profile. However, by choosing appropriate priors it might be possible to exclude such parameter values in order to avoid undersampling.

5.4 Computational feasibility

We have shown that orthonormalisations of third-order profiles can overcome the limitations of sérsiclets while preserving their mathematical justification. However, we have not yet mentioned a serious practical limitation of this novel approach: The numerical orthonormalisation of third-order profiles is computationally highly expensive. Fitting a galaxy on a, say, 100×100 pixel grid while freely adjusting all model parameters is infeasible on a standard computer. A problematic work-around could be to first fit a simple third-order profile to the galaxy and then only orthonormalise the best-fit profile in order to model the data's deviation from the mean profile. However, this step-wise approach by construction is very unlikely to find the best-fitting basis-function expansion because the first step produces a *biased* fit and *not* a mean profile. Therefore, we do not recommend this approach. Another work-around would be to set up a library of basis functions for all realistic parameter values of third-order profiles, such that numerical orthonormalisation has not to be conducted on-the fly during the fit. This approach is hampered by the fact that third-order profiles have three free parameters such that a decently detailed sampling of this three-dimensional parameter space – which is necessary in order to provide reliable fits – would produce an extensive library. The best solution is certainly to maintain the numerical orthonormalisation during the fit and to employ Graphics Processing Units (GPUs) instead of normal CPUs. For such a pure “number crunching” like numerical orthonormalisation, GPUs impressively outperform CPUs (e.g. Fluke et al. 2011).

6 CONCLUSIONS

In this article, we reinvestigated the method of sérsiclets in order to overcome the limitations of shapelets reported by Melchior et al. (2010) in parametrising galaxy morphologies. Orthogonalising the Sérsic profile is justified by the fact that the Sérsic profile is the first-order Taylor expansion of any real light profile (Appendix A1). We obtain the following results:

- From general radial light profiles like the Sérsic profile, we can only construct polar basis function because Cartesian basis functions do not exhibit the azimuthal symmetry required in the context of galaxy morphologies. Shapelets are the only exception to this rule.

- Sérsiclet basis functions exist analytically, such that no numerical orthonormalisation is required and models are simple to evaluate. Polar shapelets are a special case of the sérsiclet basis functions.

- Sérsiclets outperform shapelets in the case of edge-on discs and elliptical galaxies, providing models with substantially lower residuals. In particular, sérsiclets overcome the ring-like artefacts introduced by shapelets when fitting galaxies with steep light profiles. However, in the case of extended objects with lots of substructure, e.g., face-on spiral galaxies, shapelets are competitive.

- Sérsiclets indeed solve the problems of shapelets. However, we revealed two new problems of this approach:

- Sérsiclets are prone to undersampling effects, if galaxies are not well-resolved. Table 1 provides an estimate of the required resolution in order to avoid undersampling. This undersampling problem stems from the *polar* basis functions being evaluated on a *Cartesian* pixel grid. The problem is therefore most prominent in the central regions of the model, where unfortunately also most of the galactic light is concentrated. Undersampling gives rise to an increased uncertainty of the model parameters. For decreasing resolution, increasing parameter uncertainties render sérsiclet models less informative, which beyond some point obstructs most if not any application. If computationally feasible, the undersampling problem may be alleviated by oversampling the model, although oversampling inevitably compromises the interpretation of the expansion coefficients.

- Sérsiclets postulate a relation between steepness of the weight function and spatial scale of polynomial oscillations (cf. Sect. 2.3). However, real galaxy morphologies do not necessarily obey this relation, e.g., in the steepness of their bulge vs. the size and distribution of star-formation knots.⁷ Therefore, we have to expect modelling problems for sérsiclets, which may not have a generally predictable impact on a given application.

- We tested the performance of sérsiclets by analysing simulated weak-lensing data from the GREAT08 challenge (Bridle et al. 2009). We observed that higher-order modes do more harm than good. Given the typically low resolution of realistic weak-lensing images and the undersampling problem of sérsiclets, we have to conclude that sérsiclets are inappropriate for shear measurements in weak lensing.

We conclude that although the now formally correct sérsiclet approach appears very reasonable at first glance, it suffers from substantial problems in practice. Therefore, for every usage of sérsiclets, we recommend a critical assessment of the impact of undersampling and the postulated unphysical relation between steepness and oscillation scales onto the results.

Finally, we demonstrated that third-order Taylor expansions of galaxy light profiles can drastically improve the modelling fidelity in comparison to Sérsic profiles. If orthonormalised, third-order profiles can overcome the undersampling problem of sérsiclets and loosen the tight relation between steepness of the weight function and spatial scale of polynomial oscillations. Furthermore, they preserve the mathematical justification of sérsiclets. However, such basis functions are computationally highly demanding. In fact, they may only be feasible using appropriate computer hardware such as GPUs.

Jiménez-Teja & Benítez (2011) introduce a set of basis functions based on Chebyshev rational functions. The authors demonstrate that their method is capable of providing excellent model reconstructions of galaxies of very different morphological types with very little computational cost. Orthonormalised higher-order profiles may provide similarly good models but certainly not at a similarly low computational cost. Hence, the method of Jiménez-Teja & Benítez (2011) appears to be superior.⁸ In general, basis-function expansions can describe azimuthal structures of galaxy morphologies very accurately. However, the astrophysical interpretation of the expansion coefficients is not obvious and has to be laboriously deduced. This is a generic problem of basis-function expansions. Conversely, GALFIT3 (Peng et al. 2010) allows to directly model the azimuthal structures exhibited by galaxy morphologies, such as spiral-arm patterns. The modelling and choice of components are “guided” by astrophysical intuition. Consequently, results obtained from GALFIT3 are easier to interpret. As discussed by Jiménez-Teja & Benítez (2011), this requires substantial manual interaction of the user which is conceptually hard to automatise. The above mentioned methods highlight a fundamental conflict for any attempt of modelling galaxies. One can either seek to first optimally describe their shapes and then interpret the abstract model parameters later – or attempt to immediately explain galaxy shapes as mixtures of a limited set of physically motivated features. The sérsiclets approach provides a compromise between these two extremes, as it incorporates the flexibility and completeness of basis-function approaches and the intuition of using a weight function, which is well-adapted to galactic morphologies.

The sérsiclet code is implemented in C++ and is available on request.

⁸ Nevertheless, Chebyshev rational functions still have a long way to go. First, the choice of scale radius suggested by Jiménez-Teja & Benítez (2011) is a work-around that may erase discriminative information when it comes to classifying galaxy morphologies. Second, the authors yet have to investigate how their basis functions fare in the regime of poorly resolved galaxies which constitute the vast majority of galaxies in surveys.

⁷ In fact, this problem also applies to shapelets.

ACKNOWLEDGEMENTS

We would like to thank the anonymous referee for valuable comments and suggestions that greatly improved the readability of this paper. RA is funded by the Klaus Tschira Foundation via the Heidelberg Graduate School of Fundamental Physics (HGSFP). PM is supported by the U.S. Department of Energy under Contract No. DE-FG02-91ER40690. KJ is supported by the Emmy-Noether-programme of the DFG.

References

- Abraham, R. G., Tanvir, N. R., Santiago, B. X., et al. 1996, *MNRAS*, 279, L47
- Abraham, R. G., van den Bergh, S., & Nair, P. 2003, *ApJ*, 588, 218
- Andrae, R. & Jahnke, K. in prep.
- Andrae, R., Jahnke, K., & Melchior, P. 2010a, *MNRAS*, 1836
- Andrae, R., Melchior, P., & Bartelmann, M. 2010b, *A&A*, 522, A21+
- Andrae, R., Schulze-Hartung, T., & Melchior, P. 2010c, arXiv e-prints 1012.3754
- Barlow, R. 1993, *Statistics: A Guide to the Use of Statistical Methods in the Physical Sciences* (Wiley VCH)
- Bartelmann, M. & Schneider, P. 2001, *Phys. Rep.*, 340, 291
- Bernstein, G. M. 2010, *MNRAS*, 406, 2793
- Bernstein, G. M. & Jarvis, M. 2002, *AJ*, 123, 583
- Berry, R. H., Hobson, M. P., & Withington, S. 2004, *MNRAS*, 354, 199
- Bershady, M. A., Jangren, A., & Conselice, C. J. 2000, *AJ*, 119, 2645
- Bridle, S., Balan, S. T., Bethge, M., et al. 2010, *MNRAS*, 405, 2044
- Bridle, S., Shawe-Taylor, J., Amara, A., et al. 2009, *Annals of Applied Statistics*, 3, 6
- Chang, T., Refregier, A., & Helfand, D. J. 2004, *ApJ*, 617, 794
- Ciotti, L. & Bertin, G. 1999, *A&A*, 352, 447
- Conselice, C. J. 2003, *The Relationship between Stellar Light Distributions of Galaxies and Their Formation Histories*
- Ferry, M., Rhodes, J., Massey, R., et al. 2008, *Astroparticle Physics*, 30, 65
- Fluke, C. J., Barnes, D. G., Barsdell, B. R., & Hassan, A. H. 2011, *PASA*, 28, 15
- Graham, A. W. & Driver, S. P. 2005, *Publications of the Astronomical Society of Australia*, 22, 118
- Jiménez-Teja, Y. & Benítez, N. 2011, ArXiv e-prints
- Kelly, B. C. & McKay, T. A. 2004, *AJ*, 127, 625
- Kelly, B. C. & McKay, T. A. 2005, *AJ*, 129, 1287
- Kennicutt, Jr., R. C. 1998, *ARA&A*, 36, 189
- Lotz, J. M., Davis, M., Faber, S. M., et al. 2008, *ApJ*, 672, 177
- Lotz, J. M., Primack, J., & Madau, P. 2004, *AJ*, 128, 163
- Massey, R. & Réfrégier, A. 2005, *MNRAS*, 363, 197
- Massey, R., Rowe, B., Refregier, A., Bacon, D. J., & Bergé, J. 2007, *MNRAS*, 380, 229
- Melchior, P., Böhnert, A., Lombardi, M., & Bartelmann, M. 2010, *A&A*, 510, A75+
- Melchior, P., Meneghetti, M., & Bartelmann, M. 2007, *A&A*, 463, 1215

- Nelder, J. A. & Mead, R. 1965, *The Computer Journal*, 7, 308
- Ngan, W., van Waerbeke, L., Mahdavi, A., Heymans, C., & Hoekstra, H. 2009, *MNRAS*, 396, 1211
- Peng, C. Y., Ho, L. C., Impey, C. D., & Rix, H. 2010, *AJ*, 139, 2097
- Réfrégier, A. 2003, *MNRAS*, 338, 35
- Réfrégier, A. & Bacon, D. 2003, *MNRAS*, 338, 48
- Rosa-González, D., Terlevich, E., & Terlevich, R. 2002, *MNRAS*, 332, 283
- Sérsic, J. L. 1968, *Atlas de galaxias australes* (Cordoba, Argentina: Observatorio Astronomico, 1968)
- Simmat, E., Tuffs, R. J., & Popescu, C. C. 2010, in *American Institute of Physics Conference Series*, Vol. 1240, American Institute of Physics Conference Series, ed. V. P. Debattista & C. C. Popescu, 87–88
- Slosar, A., Land, K., Bamford, S., et al. 2009, *MNRAS*, 392, 1225
- van der Wel, A., Bell, E. F., Holden, B. P., Skibba, R. A., & Rix, H. 2010, *ApJ*, 714, 1779

APPENDIX A: SÉRSIC PROFILE AS FIRST-ORDER TAYLOR EXPANSION

We reveal the nature of the Sérsic profile as a first-order Taylor expansion. Our emphasis is on the justification of the choice of the Sérsic profile for orthogonalisation.⁹ Furthermore, we briefly outline an alternative approach to generalise Sérsic profiles by higher-order expansions.

A1 First-order expansion

Let us consider the real, two-dimensional light profile of a galaxy $I(\vec{x})$ projected onto the sky, which may exhibit arbitrary radial and azimuthal structures. Due to observational effects, e.g., noise and resolution, the observed light profile $I_{obs}(\vec{x})$ will be different. If noise and resolution have a strong impact, we cannot identify azimuthal structures anymore and only the radial decline is left, i.e., $I_{obs}(\vec{x}) \approx I_{obs}(r)$. Let us further consider a rescaling of the observed light profile $p(r) = I_{obs}(r)/I_{obs}(0)$, such that $0 < p(r) \leq 1$. Then we can take the logarithm of $p(r)$ and due to $\log p(r) \leq 0$, for $r > 0$ we can also take the logarithm a second time, introducing

$$\tilde{p}(r) = \log(-\log p(r)) . \quad (\text{A1})$$

We now Taylor expand this function $\tilde{p}(r)$ in $\log r$ at a characteristic radius $\log \beta$ to first order, i.e., a constant plus the first nontrivial term, which yields,

$$\tilde{p}(r) \approx A + B(\log r - \log \beta) = A + \log(r/\beta)^B . \quad (\text{A2})$$

Let us transform backwards now,

$$\log p(r) = -e^{\tilde{p}(r)} \approx -e^A (r/\beta)^B \quad (\text{A3})$$

and hence

$$p(r) \approx \exp \left[-e^A (r/\beta)^B \right] . \quad (\text{A4})$$

⁹ Ciotti & Bertin (1999) also investigate a Taylor-expansion of the Sérsic profile, but they expand in powers of Sérsic index and not in powers of radius.

All we need to do now is to identify the coefficients A and B of the Taylor expansion in Eq. (A2). If we simply “rename” these constants by $B = 1/n_S$ and $A = \log(b_n)$, then we have arrived at the definition of the Sérsic profile

$$p_S(r) = \exp \left[-b_n \left(\frac{r}{\beta} \right)^{1/n_S} \right]. \quad (\text{A5})$$

Evidently, the Sérsic profile is a first-order Taylor expansion at $r_0 = \beta > 0$. In other words, in the limit of low resolution and low signal-to-noise ratios (where substructures are negligible) *any* radial light profile is approximately a Sérsic profile.¹⁰ This naturally explains why the Sérsic profile is such a good fit to real galaxies in this regime. Furthermore, this also leads us to the expectation that with improving imaging quality the Sérsic profile will not be a good match anymore, because it is “only” a *first-order* expansion.

A2 Higher-order expansions

Given the fact that the Sérsic profile is the first-order Taylor expansion of a real light profile, an obvious strategy to enhance the Sérsic profile is to allow for higher orders in the Taylor expansion of Eq. (A2). However, a realistic profile has to be unity at $r = 0$ and it has to approach zero for $r \rightarrow \infty$. As the Taylor expansion is in $\log r$, only expansions where the leading order term is of odd power in $\log r$ and has a positive expansion coefficient can satisfy these constraints. Therefore, the next useful higher-order expansion beyond the Sérsic profile is a third-order expansion,

$$\tilde{p}(r) \approx A + B \log(r/\beta) + C \log^2(r/\beta) + D \log^3(r/\beta), \quad (\text{A6})$$

where $D > 0$ and A , B , and C are arbitrary.

APPENDIX B: MATHEMATICAL DERIVATION OF RADIAL PARTS OF SÉRSICLETS

In this appendix, we give the derivation of the radial part of the sérsiclets, showing that the basis functions have an analytic form. Our starting point is the scalar product of two radial modes of orders l and l' ,

$$\langle l|l' \rangle = \int_0^\infty dr r R_l(r/\beta) R_{l'}(r/\beta) \exp \left[-b \left(\frac{r}{\beta} \right)^{1/n_S} \right] \quad (\text{B1})$$

where we have adopted Dirac notation from quantum mechanics. $R_l(r)$ denotes the radial polynomials we are looking for and the Sérsic profile acts as the weight function or “metric” of this scalar product. Note the functional determinant $dr r$, which is due to our integration in polar coordinates. We now change variables according to

$$u(r) = b \left(\frac{r}{\beta} \right)^{1/n_S}, \quad (\text{B2})$$

such that

$$dr r = \beta^2 \frac{n_S}{b^{2n_S}} u^{2n_S-1} du. \quad (\text{B3})$$

¹⁰ This is not true for radial profiles that are not differentiable, i.e., where no Taylor expansion exists. However, such profiles are unphysical.

The limits of integration do not change under this transformation. Then Eq. (B1) reads

$$\langle l|l' \rangle = \beta^2 \frac{n_S}{b^{2n_S}} \int_0^\infty du \tilde{R}_l(u) \tilde{R}_{l'}(u) u^{2n_S-1} e^{-u}. \quad (\text{B4})$$

The “new” weight function of this transformed scalar product is now of the form $u^k e^{-u}$, where $k = 2n_S - 1$, and the corresponding set of orthogonal polynomials are the associated Laguerre polynomials¹¹,

$$L_l^k(u) = \frac{e^u u^{-k}}{l!} \frac{d^l}{du^l} \left(e^{-u} u^{l+k} \right). \quad (\text{B5})$$

The L_l^k exist if and only if $k > -1$. This is guaranteed, since $k = 2n_S - 1$ and the Sérsic index satisfies $n_S > 0$. The normalisation factor is

$$\int_0^\infty du L_l^k(u) L_l^k(u) u^k e^{-u} = \frac{\Gamma(l+k+1)}{l!}, \quad (\text{B6})$$

where Γ denotes the Gamma function. Consequently, the radial parts of the sérsiclets read

$$R_l(r) = \frac{1}{N_l} L_l^{2n_S-1} \left[b (r/\beta)^{1/n_S} \right] \exp \left[-\frac{b}{2} (r/\beta)^{1/n_S} \right] \quad (\text{B7})$$

with normalisation factor

$$N_l = \sqrt{\frac{\beta^{2n_S} \Gamma(l+2n_S)}{b^{2n_S} l!}}. \quad (\text{B8})$$

Mind the factor of $1/2$ in the exponent of Eq. (B9), which arises from our definition that the Sérsic profile is the weight function in Eq. (B1). We could also have defined Eq. (B9) with a pure Sérsic profile, resulting in a factor 2 arising in Eq. (B1). Fit results obtained from both definitions will not differ, since these factors are absorbed in the parameter b .

In the special case of polar shapelets these expressions simplify. First, for $n_S = 0.5$, we note that $k = 2n_S - 1 = 0$, which implies $\Gamma(l+k+1) = \Gamma(l+1) = l!$ and simplifies the associated Laguerre polynomial L_l^k to the “normal” Laguerre polynomial $L_l^0 = L_l$. Second, in order to obtain shapelets, we need to set $b = 1$. Therefore, the radial parts of polar shapelets read

$$R_l(r) = \frac{1}{\sqrt{\beta^2/2}} L_l \left[(r/\beta)^2 \right] \exp \left[-\frac{r^2}{2\beta^2} \right]. \quad (\text{B9})$$

The basis functions introduced by Massey & Réfrégier (2005) as “polar shapelets” (their Eq. (8)) differ from Eq. (B9) by using $x^{|m|} L_{(l-|m|)/2}^{|m|}(x^2)$ instead of $L_l(x^2)$. Their basis functions are not orthogonal, e.g., consider

$$\langle l=1, m=1 | l=2, m=0 \rangle \propto \int_0^\infty dr r e^{-r^2} r^{11} L_0^1(r^2) r^{10} L_1^0(r^2), \quad (\text{B10})$$

which equals $-\sqrt{\pi}/8$ and is thus non-zero. Consequently, the “polar shapelets” defined by Massey & Réfrégier (2005) are incorrect. However, the linear independence is preserved because no two states with identical values of m (otherwise the azimuthal parts $e^{im\varphi}$ would differ) and different values of l can have identical $x^{|m|} L_{(l-|m|)/2}^{|m|}(x^2)$.

¹¹ <http://mathworld.wolfram.com/LaguerrePolynomial.html>

APPENDIX C: OPTIMISATION PROCEDURE

Having defined sérsiclet models, we also need to clarify how to fit such models to given imaging data.

C1 Maximum-likelihood solution

For the moment, we assume that we are given estimates of the nonlinear model parameters $(N_{\max}, n_S, \beta, \vec{x}_0, \epsilon)$. We define a vector \vec{c} of free parameters that form the coefficients. Furthermore, we write the image as a vector \vec{y} of size N , where N denotes the number of pixels in the given image. Finally, we define the so-called $N \times P$ design matrix X , such that X_{np} is the p -th basis function evaluated at the n -th image pixel (after forward convolution with the PSF). With these definitions, we define the residual vector

$$\vec{R} = \vec{y} - X \cdot \vec{c}, \quad (\text{C1})$$

which is an vector of size N itself. Here “ \cdot ” denotes matrix multiplication. As the pixel noise of modern imaging data is usually Gaussian in excellent approximation, we are allowed to define

$$\chi^2 = \vec{R}^T \cdot \Sigma^{-1} \cdot \vec{R}, \quad (\text{C2})$$

where Σ denotes the $N \times N$ pixel covariance matrix. In the case of uncorrelated Gaussian noise with constant variance σ^2 in all pixels, Σ takes the simple form $\Sigma = \text{diag}(\sigma^2, \dots, \sigma^2) = \sigma^2 I$. It is straightforward to show that the maximum-likelihood estimate that minimises χ^2 is

$$\hat{\vec{c}} = (X^T \cdot \Sigma^{-1} \cdot X)^{-1} \cdot X^T \cdot \Sigma^{-1} \cdot \vec{y}. \quad (\text{C3})$$

The matrix $X^T \cdot \Sigma^{-1} \cdot X$ has a special meaning: It is the $P \times P$ covariance matrix of the coefficients \vec{c} , which would follow from a Fisher analysis. In this formalism, we get this information for free.

The advantage of expressing the maximum-likelihood solution in terms of matrix operations is that we can employ fast and efficient linear-algebra algorithms. In our case, the basis functions are implemented in C++ and we use wrapper classes to import the packages ATLAS¹² and LAPACK¹³.

C2 Optimising the nonlinear parameters for given N_{\max}

We now assume that we are given an estimate of the maximum order, N_{\max} , and need to get estimates of $(n_S, \beta, \vec{x}_0, \epsilon)$. These estimates are derived from a Simplex algorithm (Nelder & Mead 1965) that we incorporate from the GNU Scientific Library (GSL)¹⁴. The Simplex algorithm is an iterative optimisation algorithm that does not employ derivatives but only evaluations of χ^2 . We also employ priors in order to restrict the model parameters to reasonable values. These priors in detail ensure that:

- The Sérsic index is in the range $0.1 \leq n_S \leq 8$.
- The scale radius satisfies $\beta > 0$.
- The object centroid \vec{x}_0 is within the pixel grid.
- The complex ellipticity satisfies $|\epsilon| < 1$.

Within these reasonable parameter ranges, we employ flat priors.

C3 Estimating the maximum order

In the case of shapelets, the maximum order, N_{\max} , is estimated via a reduced χ^2 . However, demanding that χ^2 equals the number of degrees of freedom is justified if *and only if* the model is purely linear (e.g., Barlow 1993; Andrae et al. 2010c). In the case of sérsiclets, this assumption is definitely violated, since sérsiclets contain many nonlinear fit parameters. We rather recommend to estimate N_{\max} by comparing the normalised residuals for models of different maximum orders. The optimal N_{\max} is then defined by the model whose normalised residuals are closest to a Gaussian with mean zero and variance one (Andrae et al. 2010c).

Concerning large samples of galaxy images, one can also decompose all objects using identical N_{\max} . This approach may be favourable because many techniques to analyse the resulting catalogue of models require that all coefficient vectors have the same dimensionality (e.g. clustering analysis, cf. Kelly & McKay 2004, 2005; Andrae et al. 2010b).

This paper has been typeset from a \TeX / \LaTeX file prepared by the author.

¹² <http://math-atlas.sourceforge.net>

¹³ <http://www.netlib.org/lapack/>

¹⁴ <http://www.gnu.org/software/gsl/manual/>